Supplementary material for

The West Kunlun Glacier Anomaly and Its Response to Climate Forcing during 2002–2020

Jianwei Luo[1,2,3], Chang-Qing Ke[1,2,3*], Thorsten Seehaus[4]

[1]Jiangsu Provincial Key Laboratory of Geographic Information Science and Technology, Key Laboratory for Land Satellite Remote Sensing Applications of Ministry of Natural Resources, School of Geography and Ocean Science, Nanjing University, Nanjing, Jiangsu 210023, China; ljwwmn@smail.nju.edu.cn

[2] Jiangsu Center for Collaborative Innovation in Novel Software Technology and Industrialization, Nanjing, Jiangsu 210023, China

[3] Collaborative Innovation Center of South China Sea Studies, Nanjing, Jiangsu 210023, China

[4]Institute of Geography, Friedrich-Alexander-Universität Erlangen-Nürnberg, 91054 Erlangen, Germany; thorsten.seehaus@fau.de

[*]Correspondence: kecq@nju.edu.cn

This file includes:

Supplementary Methods

1. Smoothing holes-filled glacier elevation change maps

In this study, we used mean difference of each elevation band to fill its corresponding gap in the dhdt map. However, this leaves abrupt gaps in maps of glacier elevation change, compared with nearest areas, which is a barrier to estimating glacier elevation change. Generally speaking, despite the fact that ice flow is much more obvious in West Kunlun (WK) than other regions in the High Mountain Asia (HMA), except Karakoram [1], we believe that glacier dynamics are continuous and extendable rather than suddenly ceasing or halting at certain points on glacier surface. Based on this, sudden elevation changes on glacier surfaces in the local study area are neither reasonable nor rational (Figure S1). Thus, we applied a smoothing approach to eradicate these abnormal sudden elevation changes on the glacier surfaces, to some extent, using Equation (1).

$$x_{i_0}y_{j_0} = \frac{\sum_{j=j_0-r+1}^{j_0+r-1}(\sum_{i=i_0-r+1}^{i_0+r-1} x_i y_i + x_{i_0+r}y_{j_0} + x_{i_0-r}y_{j_0} + x_{i_0}y_{j_0+r} + x_{i_0}y_{j_0-r})}{[2(r-1)+1]^2+4} \quad (1)$$

where $x_{i_0}y_{j_0}$ represents pixels in the gap-filled glacier area waiting to be smoothed, r represents radius distance in the unit of pixel number, i and j represent pixel location in glacier elevation change maps.

Supplementary Discussions

1. ASTER images time offsets

In this study, we used multi-temporal ASTER images to obtain glacier elevation at certain time points (i.e., 2002, 2011, and 2020). Therefore, it was essential for us to deal with the time offset. We apply a method similar to that of [2]. Firstly, we excluded pixels obscured due to cloud impact. Afterwards, we clipped ASTER DEMs to eliminate overlap between neighboring ASTER DEMs within each time span. Finally, we used mosaic imagery from 2001, 2002, 2003, 2004, and 2005 to construct the ASTER DEM map for 2002. The same procedure was applied to DEM files for 2010–2013 and 2019–2021. Finally, we obtained mosaiced ASTER DEMs for 2002, 2011, and 2020. The

results of this procedure can be seen in Figure S2-S4. When calculating glacier elevation change for each glacier during 2002–2011, 2011–2020, and 2002–2020, we took advantage of time intervals for each glacier. For instance, if a glacier was covered by ASTER DEM in 2001, 2012, and 2021, we assumed time offsets of 11 years, 9 years, and 20 years, respectively. More information about ASTER image coverage in each time span can be seen in Table S1-3.

2. Correlations and significances of surface temperature and IVT trends

We applied the OLS model to analyze annual JJA surface temperature, annual summer surface temperature (JJA surface temperature), annual IVT, summer IVT (JJA IVT), and winter IVT (DJF IVT) trends in WK. Thus, it was essential for us to depict correlation (coefficient R) and significance (P value) per pixel [3]. JJA and DJF IVT trend maps can be seen in Figures S5 and S6. Correlation (Spearman's r) per pixel of summer surface temperature, winter surface temperature, annual IVT, JJA IVT, and DJF IVT trends can be seen in Figures S7–S11. Significance per pixel of summer surface temperature, winter surface temperature, annual IVT, JJA IVT, and DJF IVT trend maps can be seen in Figures S12-S16. In addition, we also portray integrated water vapor transport direction (IVT) (Figure S17).

3. Other climatic factors analysis

[4] assumed that annual range of monthly surface temperature (surface temperature range) and ratio of summer precipitation (JJA precipitation ratio) correlate well with glacier elevation changes in HMA. Therefore, we calculated annual trends of these two climatic factors (Figure S18-S19). We found that annual surface temperature range can explain the different SMB patterns between western and eastern WK. We also found that JJA precipitation in WK tended to display a decline over the past 20 years, which can explain the slight mass loss in WK during 2002–2020. Correlations (R) and significances (P) of annual surface temperature and summer IVT can be seen from Figures S20-S23.

4. Linear and nonlinear glacier SMB sensitivity to climate factors

[5] confirmed with deep learning technology that glacier mass balance sensitivity to climatic forcing is nonlinear. In this study, we compared glacier SMB response to summer surface temperature and IVT using the ordinary least square (OLS) model and an Artificial Neural Network (ANN) model [6].

To investigate the linear nature of glacier SMB sensitivity in WK, we calculated glacier SMB, summer surface temperature, and IVT for each glacier. After that, we calculated correlation coefficient (Spearman's R) between glacier SMB and JJA surface temperature and annual IVT in WK during 2002–2011, 2011–2020, and 2002–2020 [4] (Figure S24). However, when we estimated coefficients and significances, we found that the ERA5.1 reanalysis dataset contained errors, thus it was necessary to exclude some unexpected errors caused by glacier mass balance estimation and meteorological elements (JJA skin temperature and annual IVT) (see Table S4).

We found that there was significant correlation and significance between glacier SMB and summer surface temperature during 2002–2011 ($R = -0.75$, $P < 0.001$) and 2011–2020 ($R = -0.72$, $P < 0.001$). Compared with summer surface temperature, glacier SMB sensitivity to IVT was less remarkable during 2002–2011 ($R = 0.28$, $P < 0.001$) and 2011–2020 ($R = 0.24$, $P < 0.001$). However, during the full period 2002–2020, the impact on glacier SMB variations of IVT ($R = 0.25$, $P < 0.001$) was more significant than summer surface temperature ($R = -0.18$, $P < 0.01$).

The final results show that the difference between linear and nonlinear glacier SMB response is trivial, but the significance of the ANN model is that it captured the over- or under-sensitivity of glacier SMB to extreme positive and negative summer surface temperature and IVT, which will help us to better constrain future glacier SMB variations.

5. Linear and nonlinear glacier ELA sensitivity to climate factors

To research linear glacier ELA sensitivity in WK to JJA surface temperature and annual IVT during 2002–2020, we calculated correlation coefficient (Spearman's R) between changes in ELA and meteorological elements (JJA surface temperature and

annual IVT) [7-9] (Figure S25). Based on this, we applied an ELA sensitivity model to establish the quantitative relationship between ELA shift and JJA surface temperature and annual IVT (see Table S5).

Meanwhile, we also aimed to depict nonlinear glacier ELA responses to atmospheric forcing (JJA surface temperature and IVT). The final results show that glacier ELA sensitivity displayed by the ANN model was more accurate than that obtained by the OLS model.

Supplementary Figures

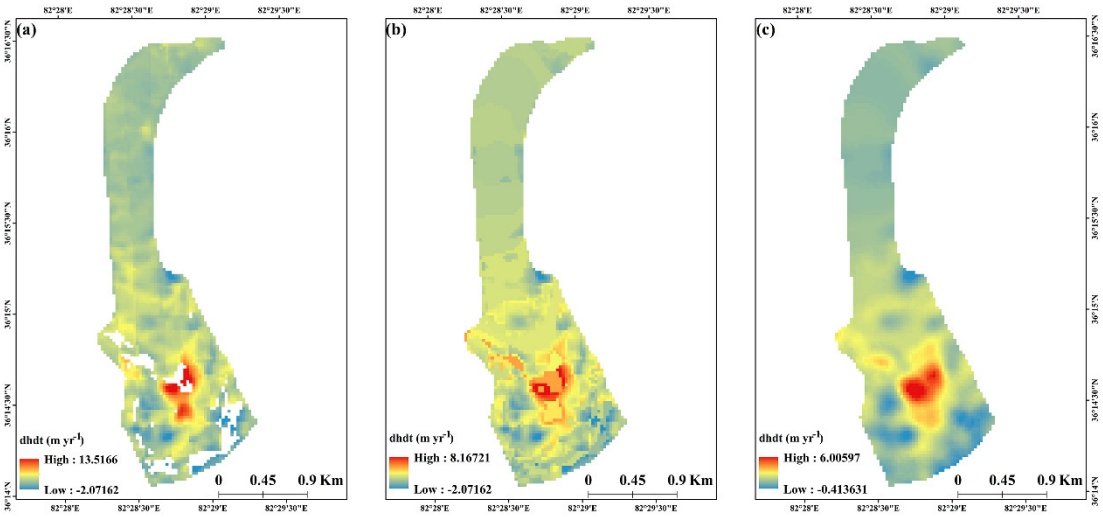

Figure S1. Comparisons between (a) original, (b) inpainting, and (c) smoothing dhdt maps. For the original dhdt map, outliers were removed from outside the reasonable glacier elevation range [10] and slope range [11]. The inpainting dhdt map used mean dhdt of each 50 m-elevation band to fill the corresponding gap due to outliers in the original dhdt map and pixel value > 3σ at each 50 m altitude bin. For the final dhdt map, the manipulating smoothing approach was applied, described in the Supplementary Method Section. The results indicate for (a): mean dhdt is

1.77 m and its standard deviation is 1.25 m; for (b): mean dhdt is 1.66 m and its standard deviation is 0.98 m; for (c): mean dhdt is 1.67 m and its standard deviation is 0.80 m.

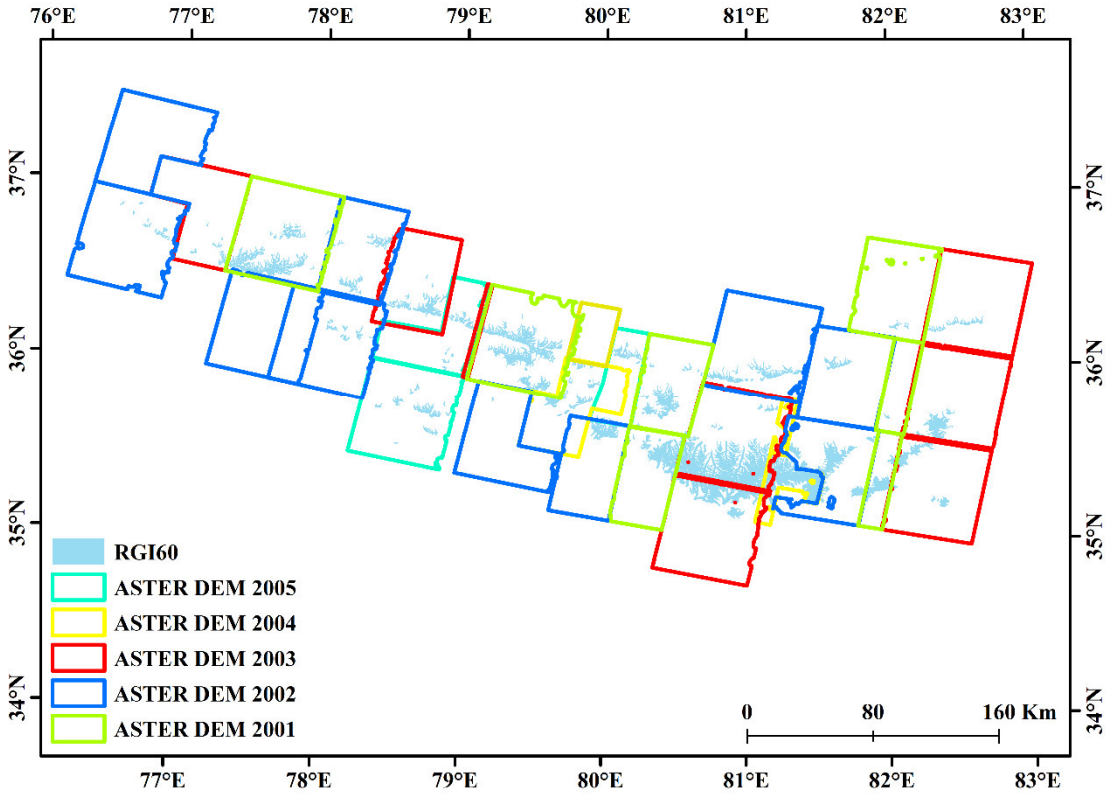

Figure S2. ASTER DEMs coverage from 2001 to 2005.

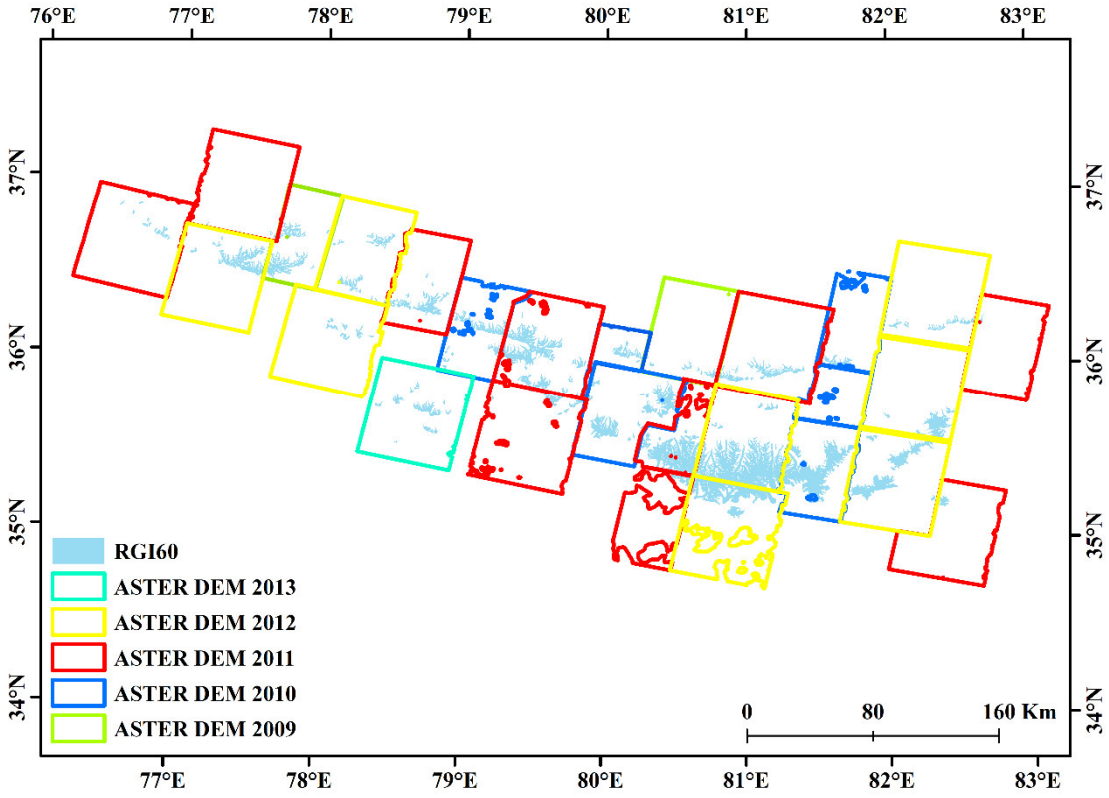

Figure S3. ASTER DEMs coverage from 2009 to 2013.

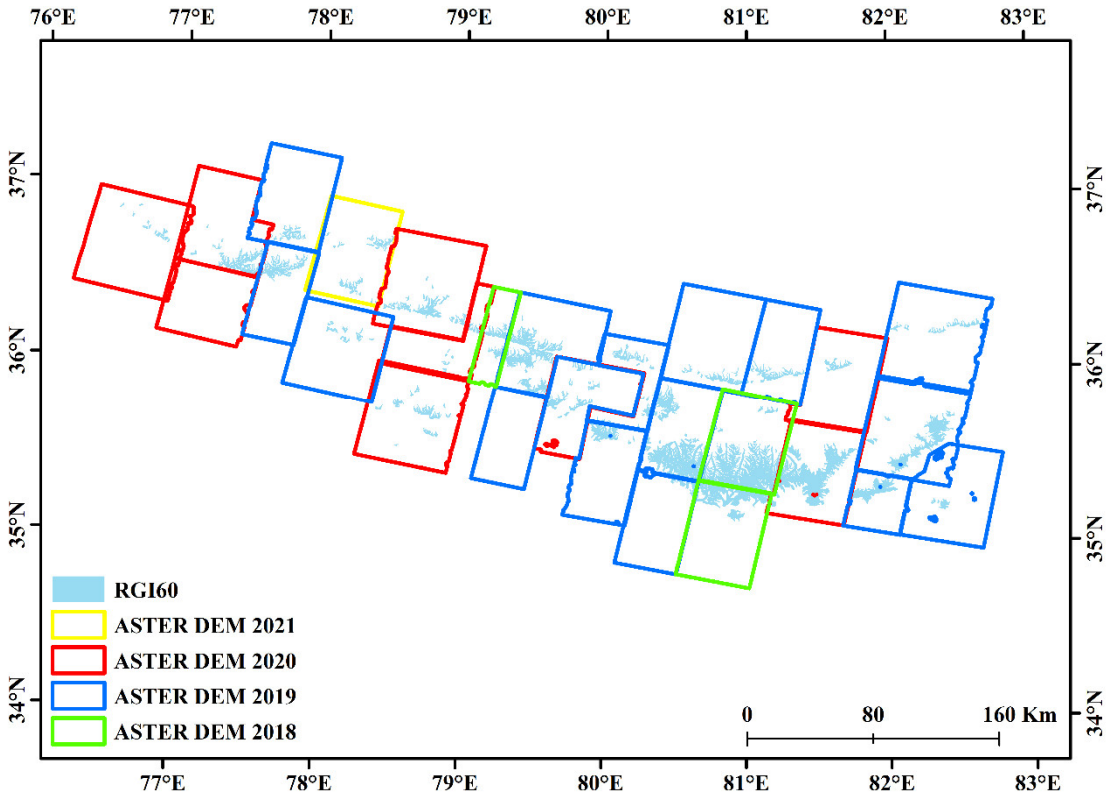

Figure S4. ASTER DEMs coverage from 2018 to 2021.

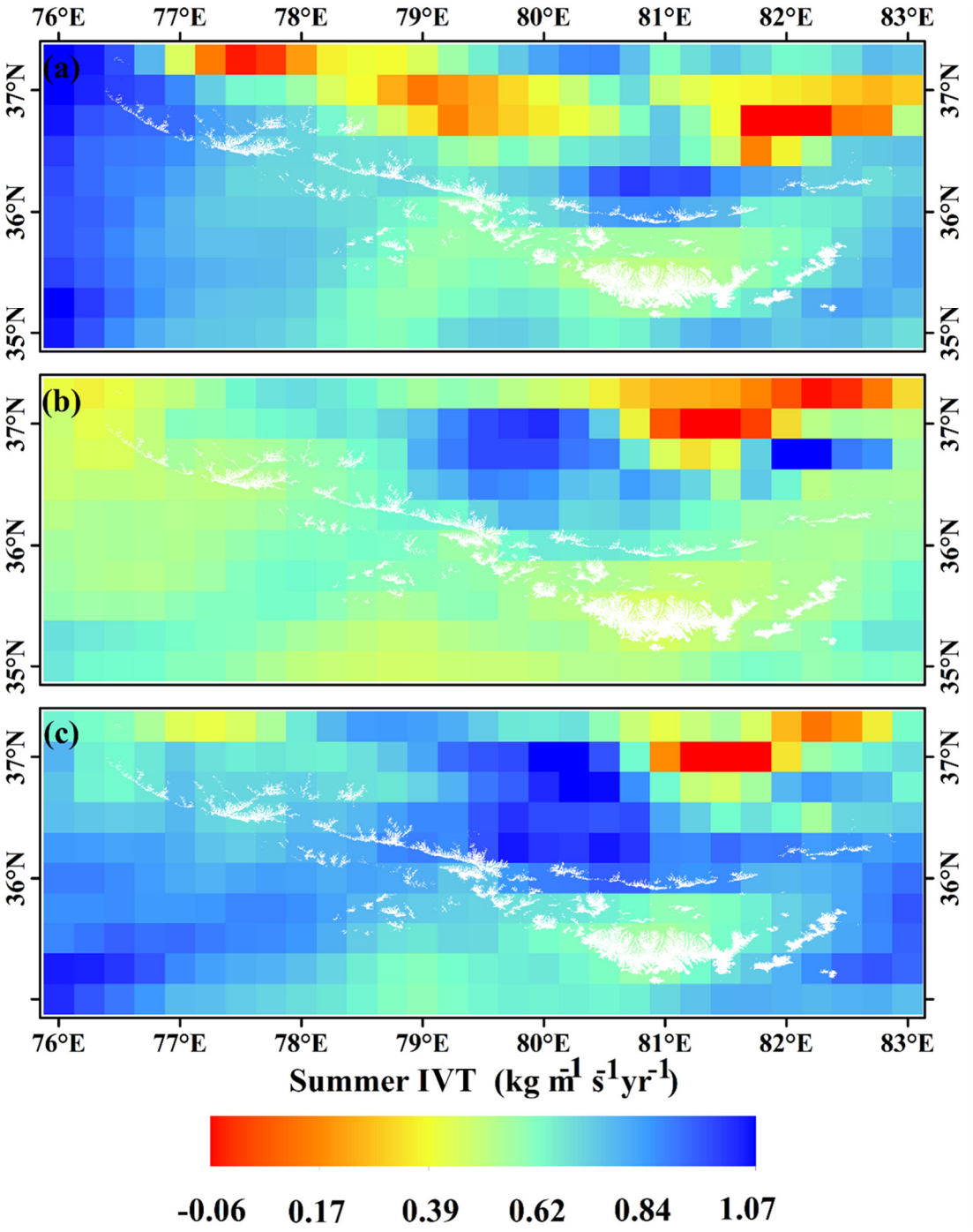

Figure S5. JJA IVT trend in WK during 2002–2011 (a), 2011–2020 (b), and 2002–2020 (c).

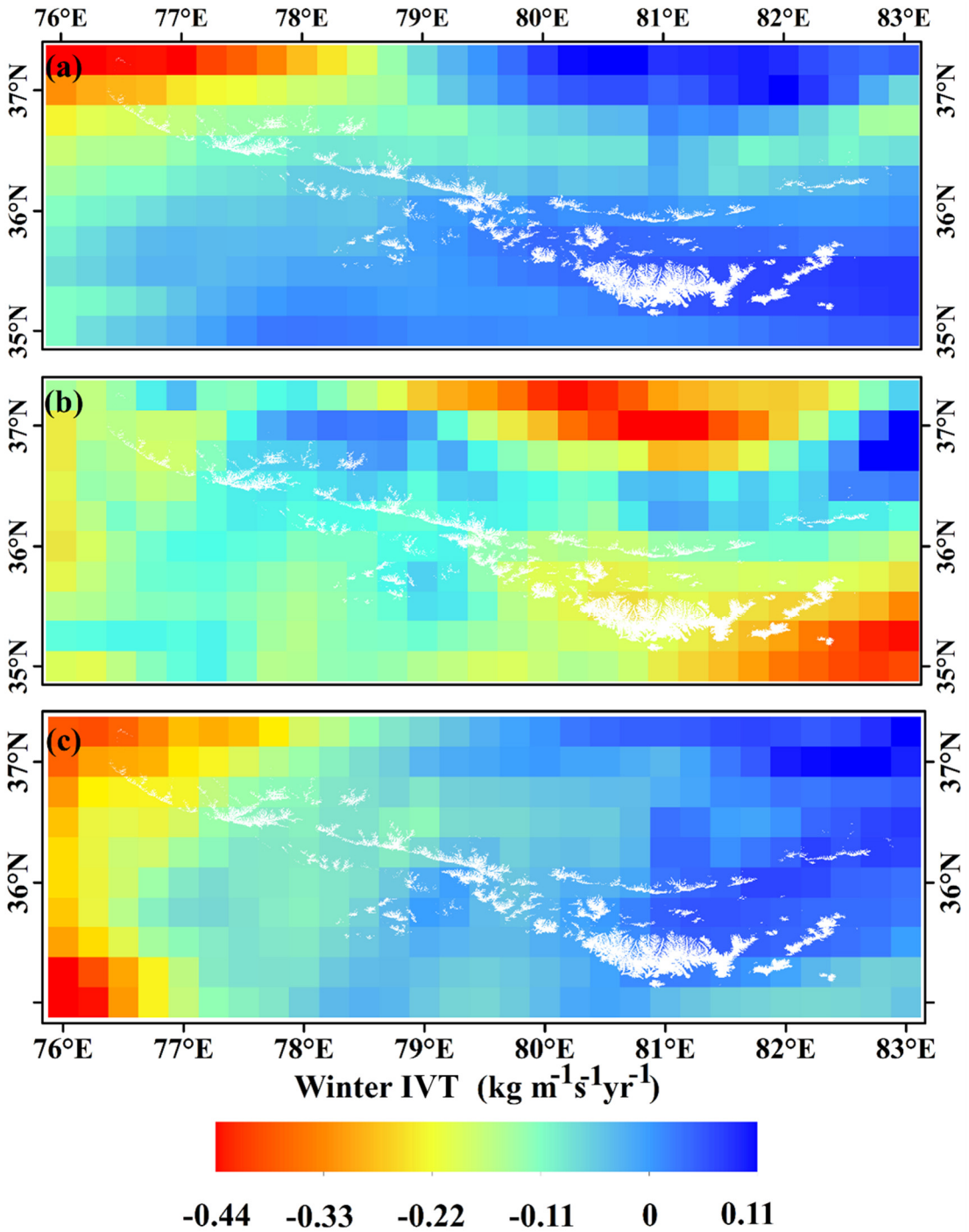

Figure S6. DJF IVT trend in WK during 2002–2011 (a), 2011–2020 (b), and 2002–2020 (c).

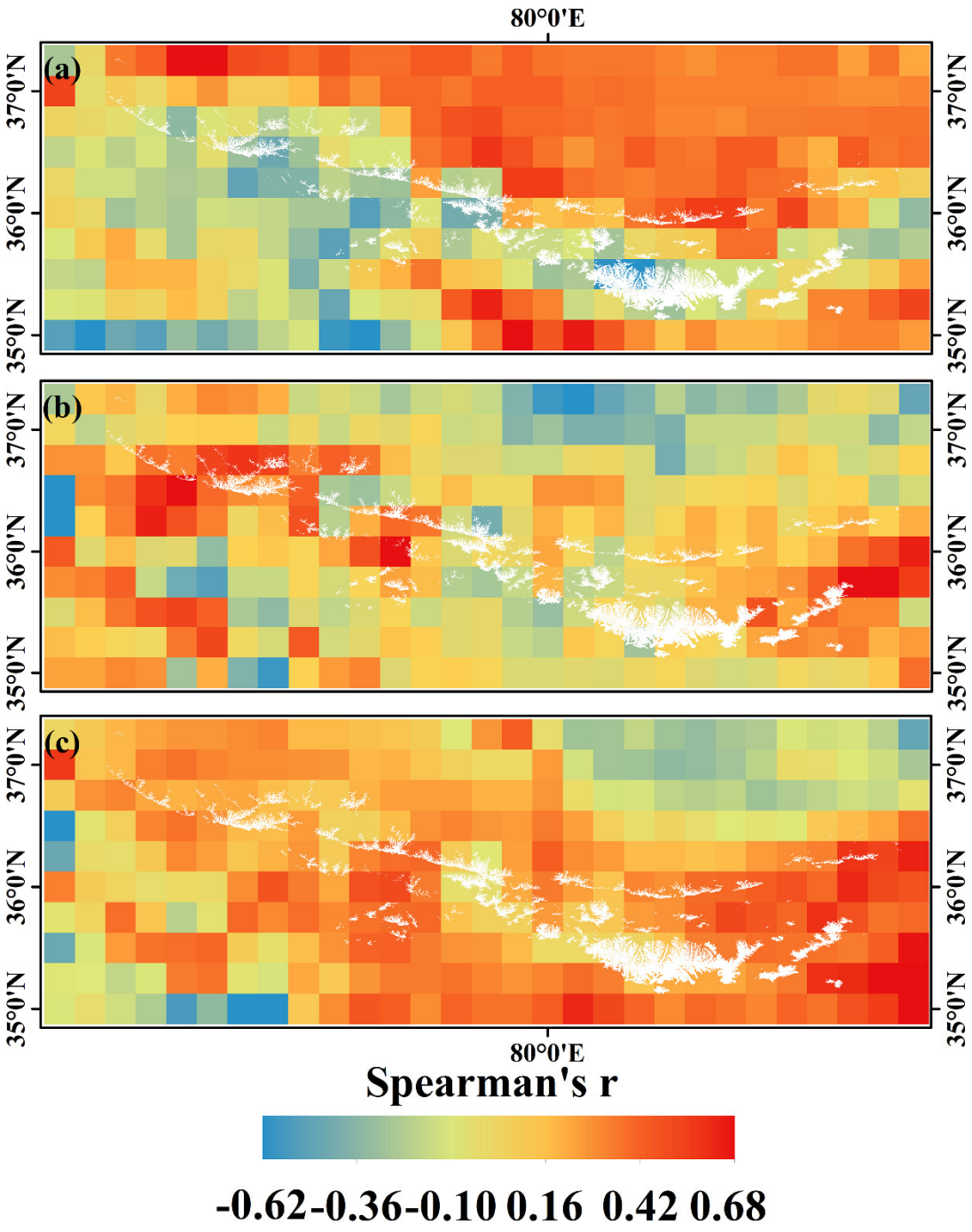

Figure S7. Correlation efficient (Spearman's R) of JJA skin temperature in WK during 2002–2011 (a), 2011–2020 (b), and 2002–2020 (c).

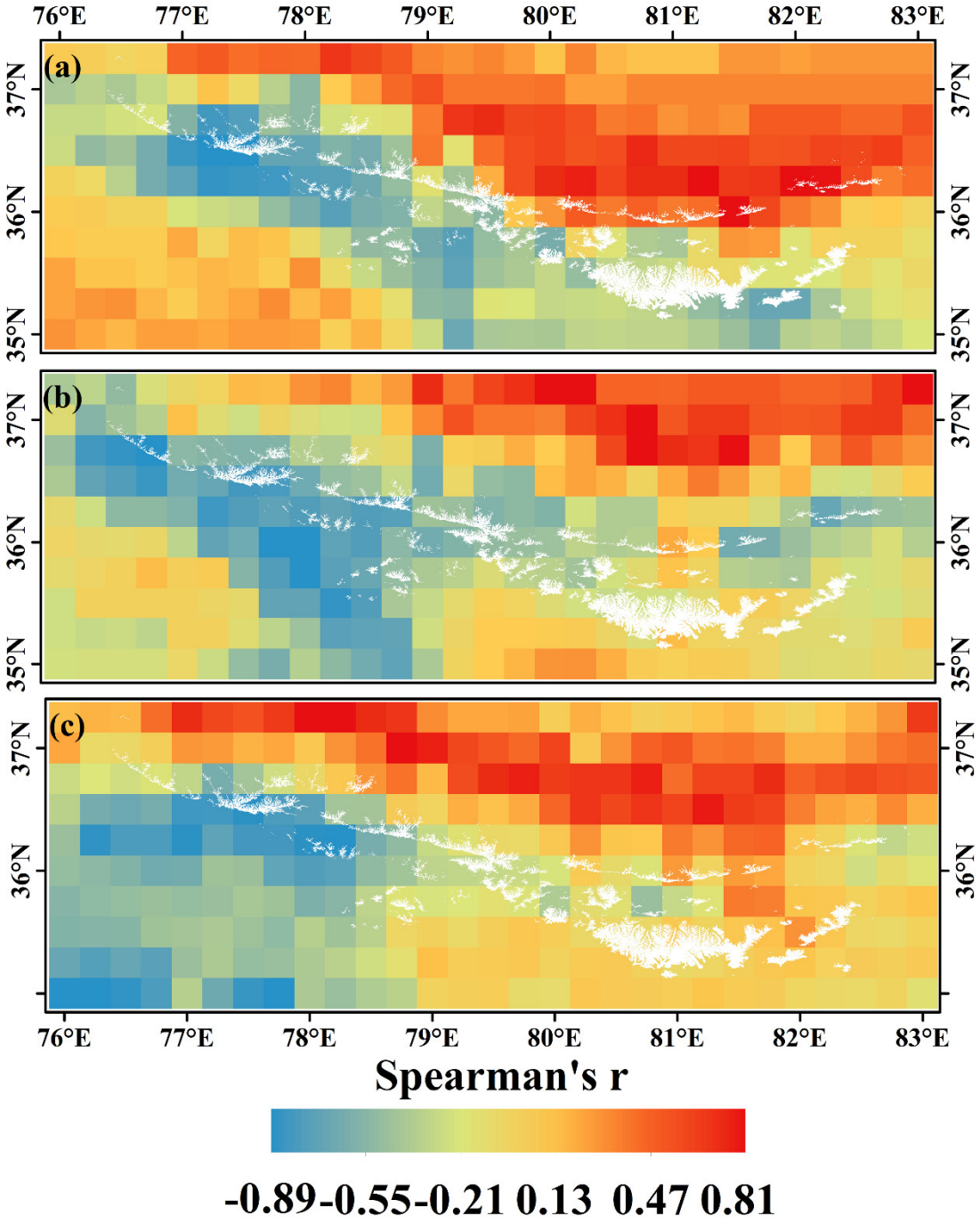

Figure S8. Correlation efficient (Spearman's R) of DJF surface temperature in WK during (a) 2002–2011, (b) 2011–2020, and (c) 2002–2020.

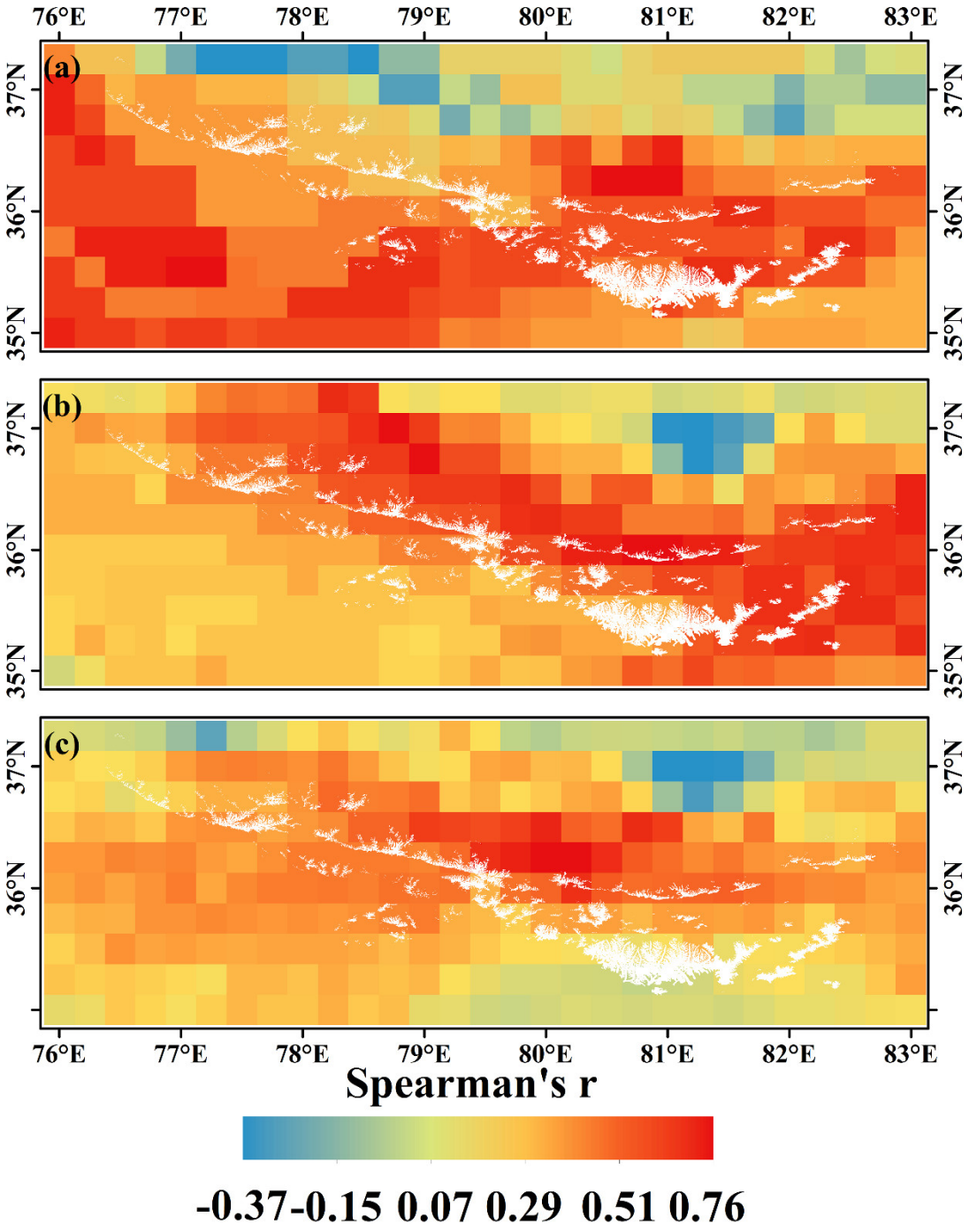

Figure S9. Correlation efficient (Spearman's R) of annual IVT in WK during (a) 2002–2011, (b) 2011–2020, and (c) 2002–2020.

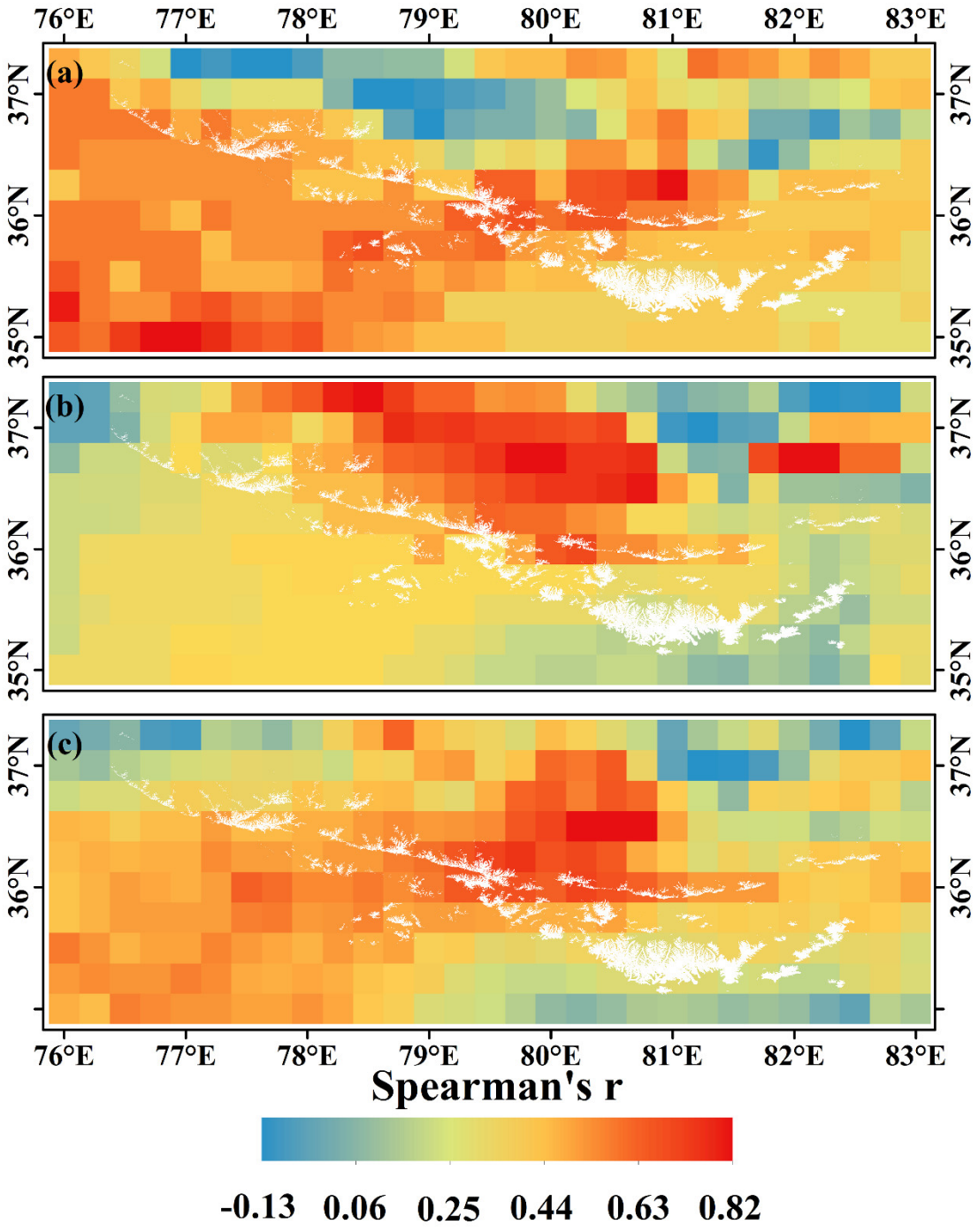

Figure S10. Correlation efficient (Spearman's R) of JJA IVT in WK during (a) 2002–2011, (b) 2011–2020, and (c) 2002–2020.

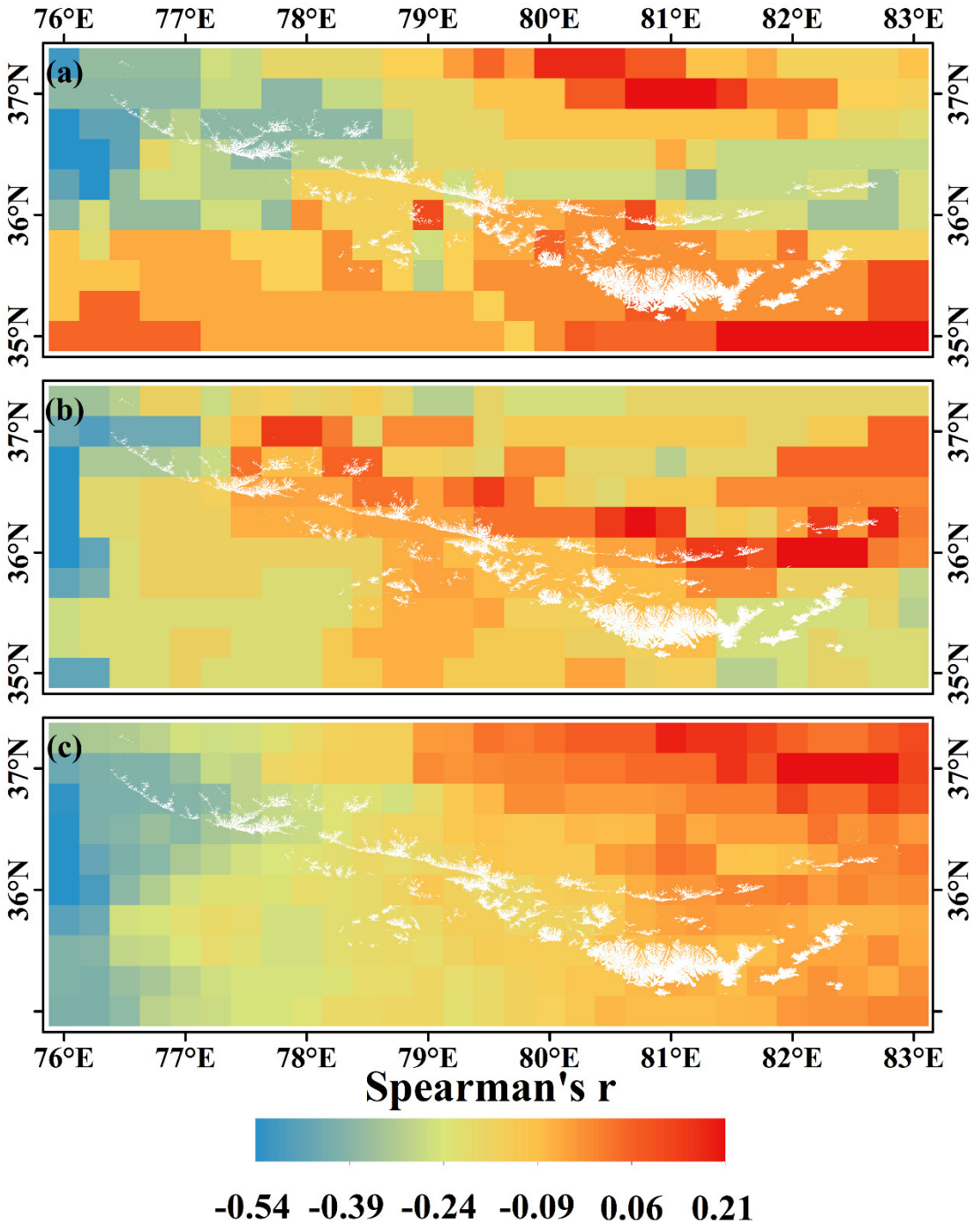

Figure S11. Correlation efficient (Spearman's R) of DJF IVT in WK during (a) 2002–2011, (b) 2011–2020, and (c) 2002–2020.

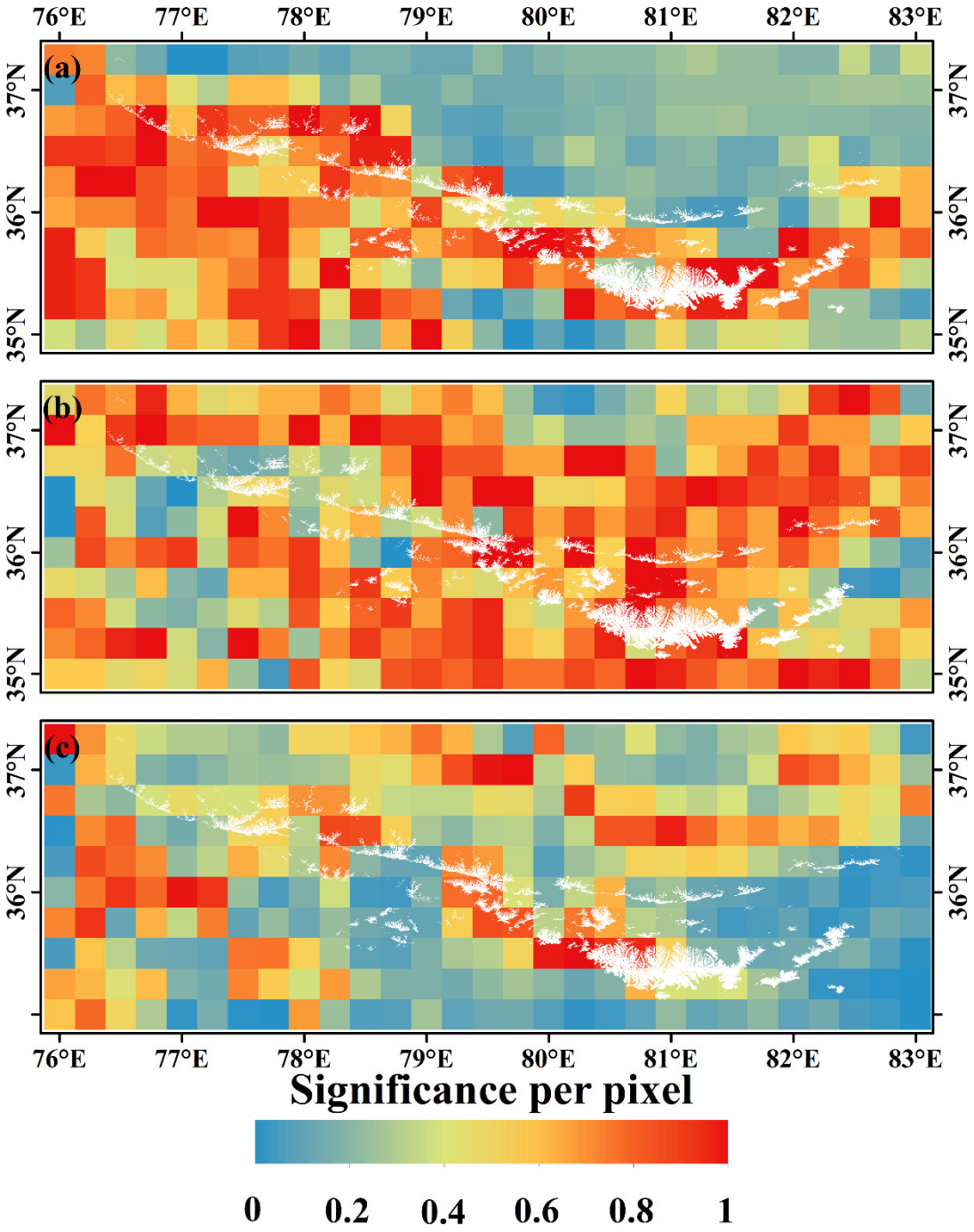

Figure S12. Significance (*p*-value) of JJA surface temperature per pixel in WK during (a) 2002–2011, (b) 2011–2020, and (c) 2002–2020.

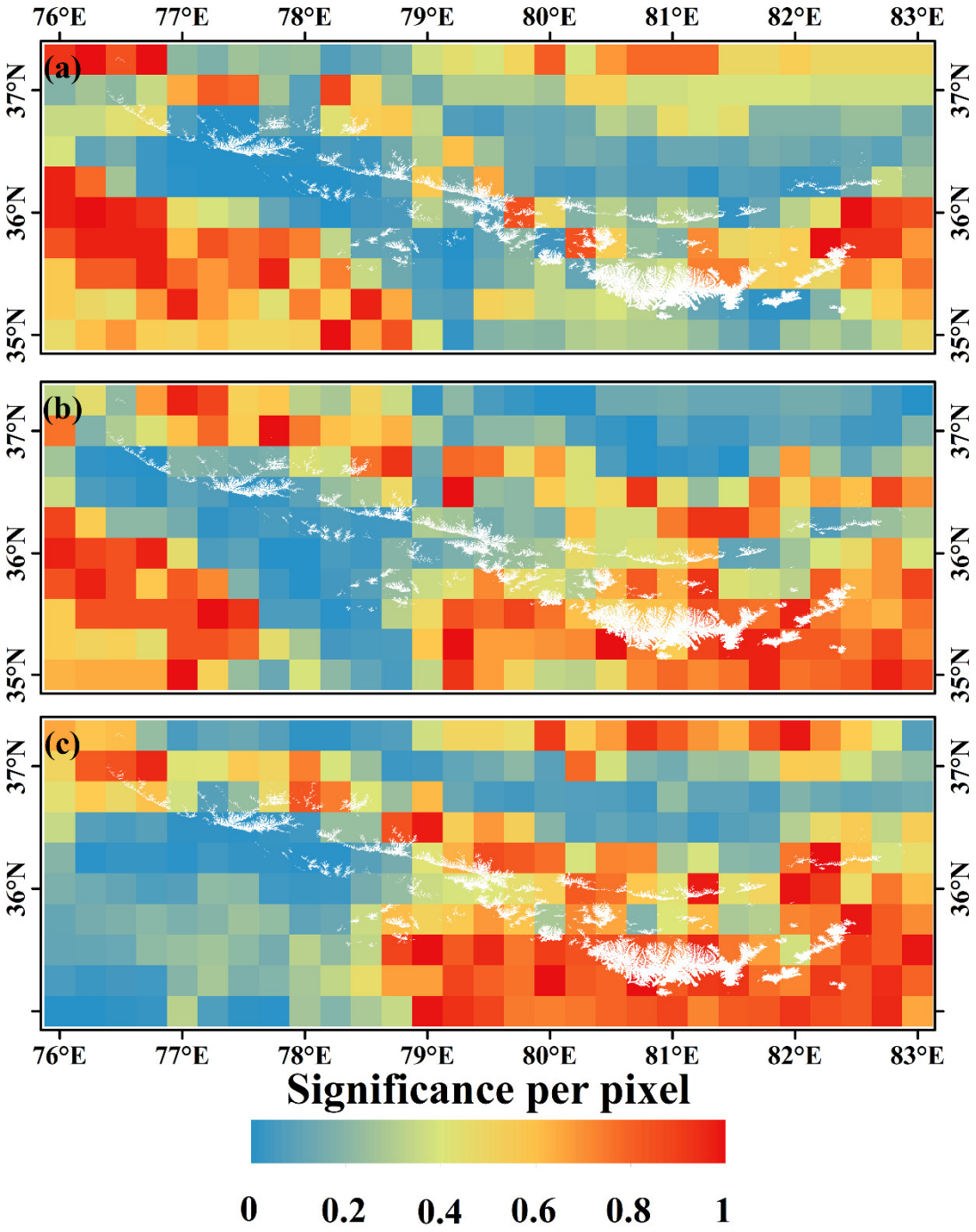

Figure S13. Significance (*p*-value) of DJF surface temperature per pixel in WK during (a) 2002–2011, (b) 2011–2020, and (c) 2002–2020.

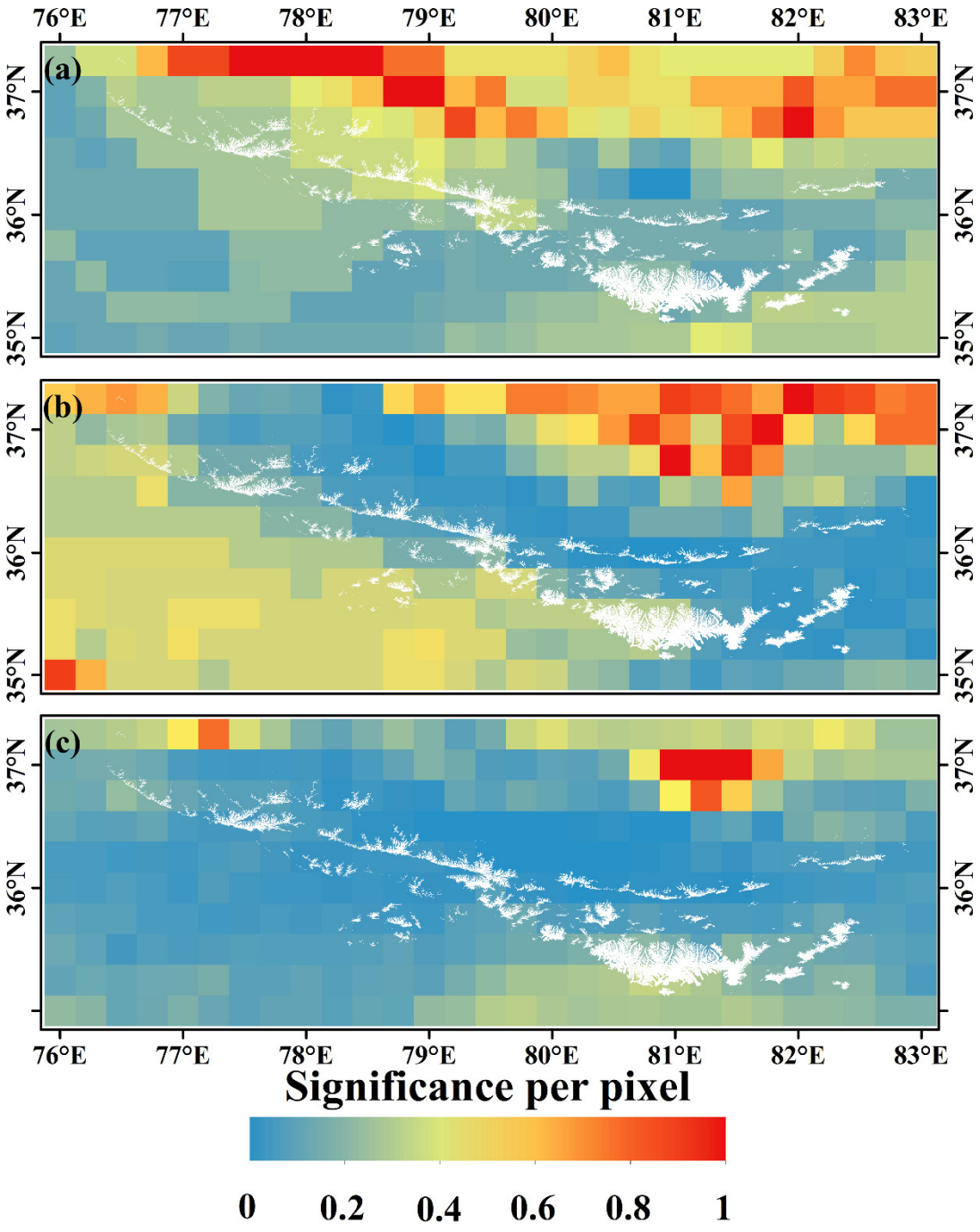

Figure S14. Significance (*p*-value) of annual IVT per pixel in WK during (a) 2002–2011, (b) 2011–2020, and (c) 2002–2020.

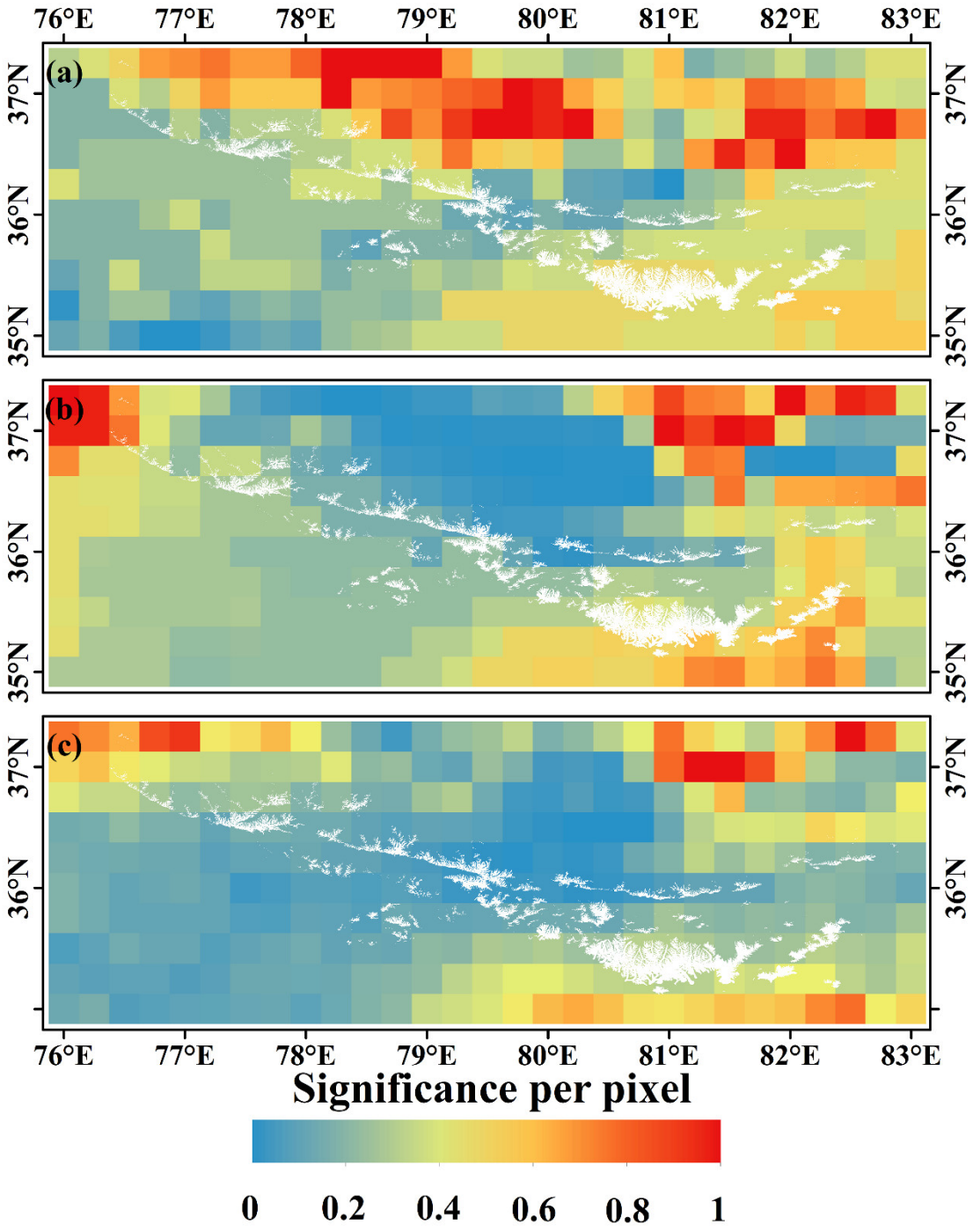

Figure S15. Significance (*p*-value) of JJA IVT per pixel in WK during (a) 2002–2011, (b) 2011–2020, and (c) 2002–2020.

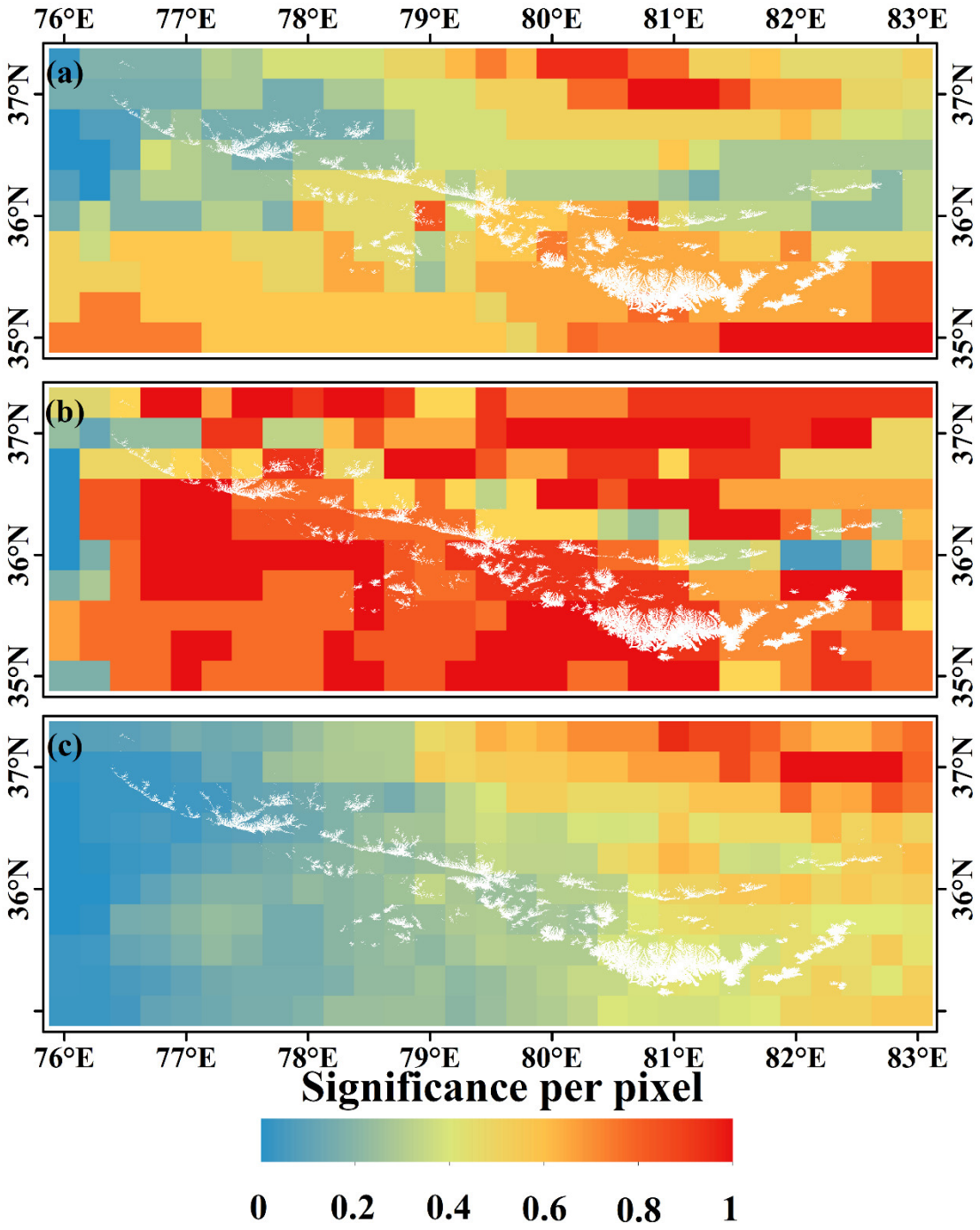

Figure S16. Significance (*p*-value) of DJF IVT per pixel in WK during (a) 2002–2011, (b) 2011–2020, and (c) 2002–2020.

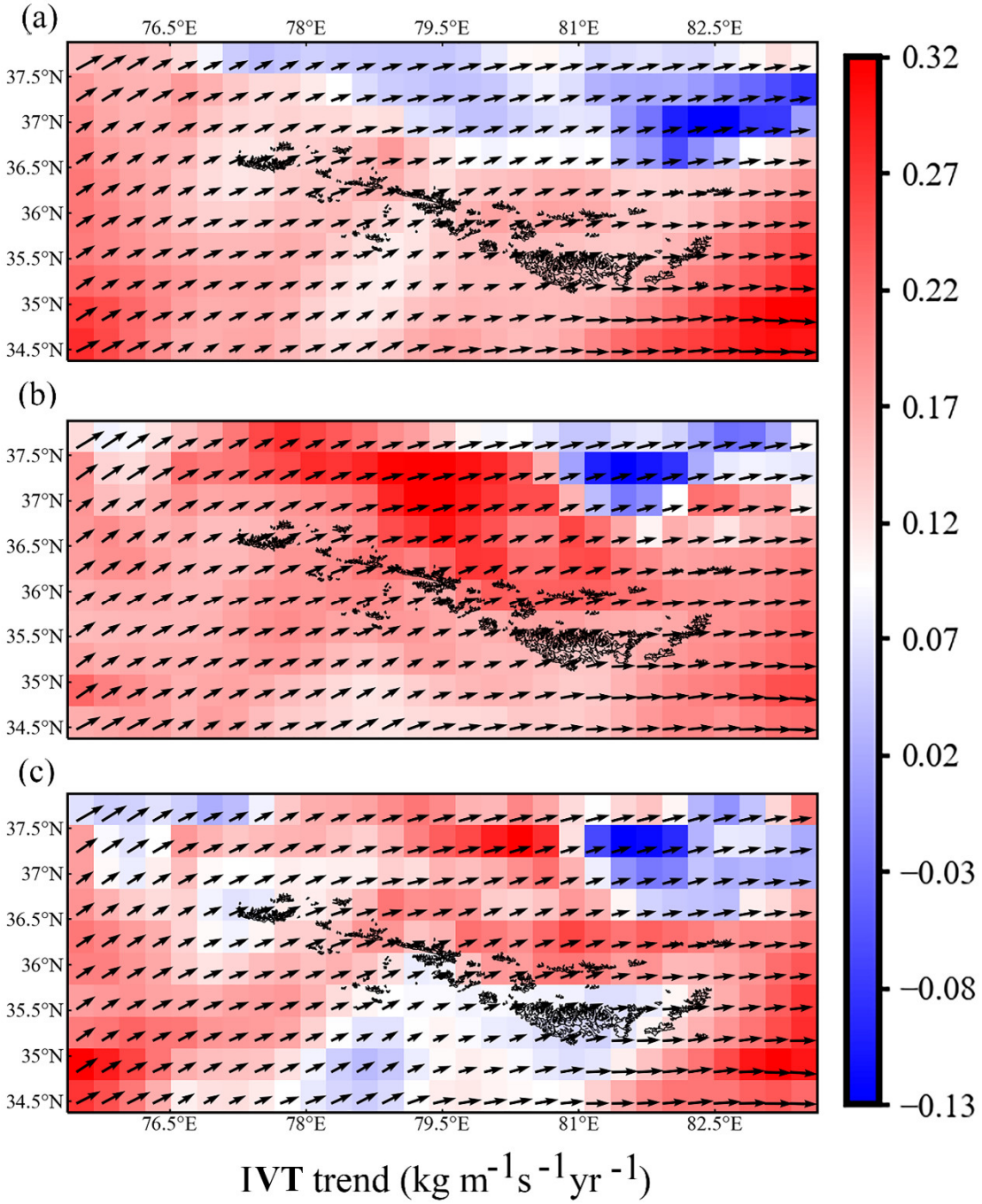

Figure S17. Annual IVT trends in WK during (a) 2002–2011, (b) 2011–2020, and (c) 2002–2020. The arrows represent the directions of IVT in each pixel. The black line represents glacier area (RGI v6.0).

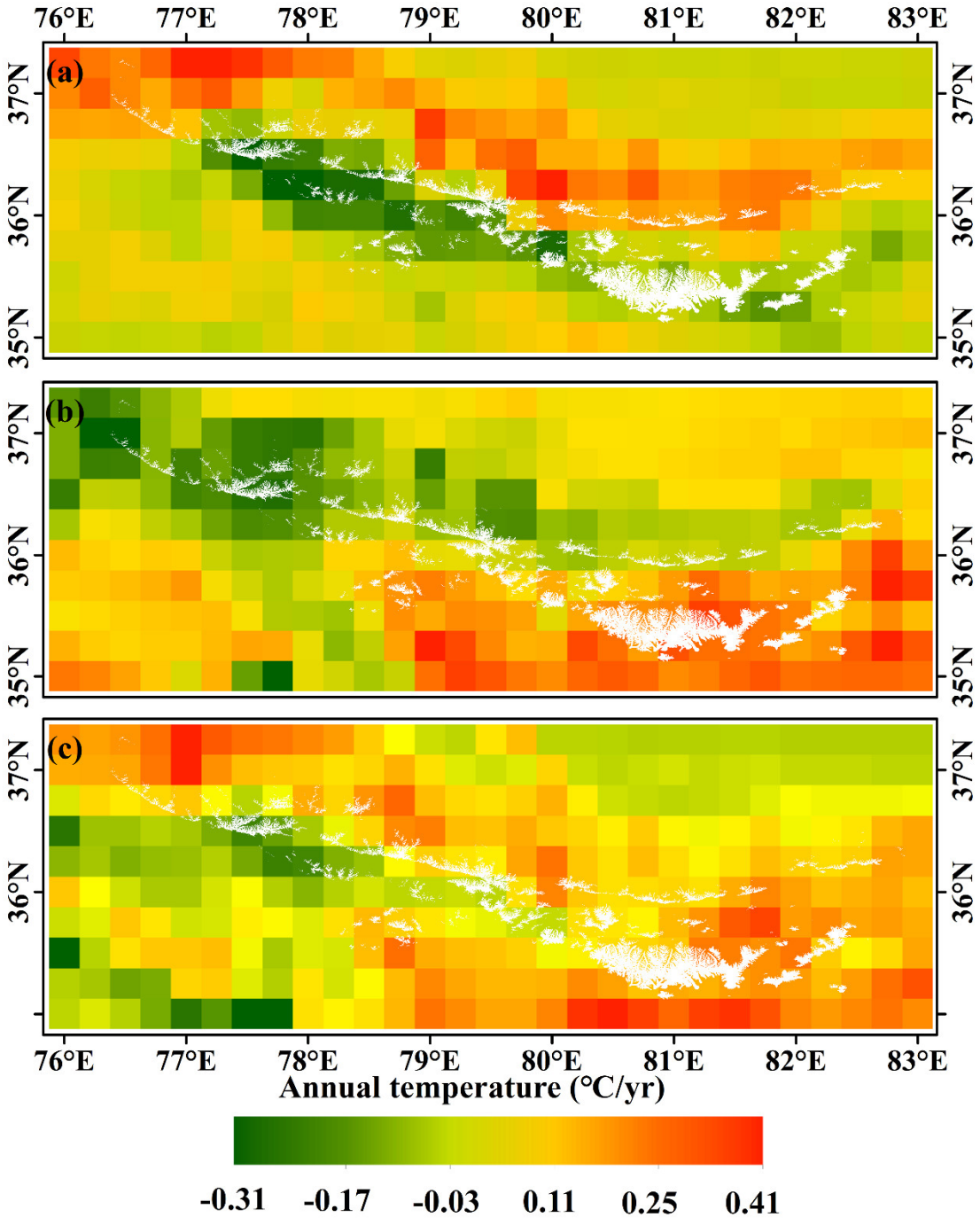

Figure S18. Annual mean surface temperature trend per pixel in WK during (a) 2002–2011, (b) 2011–2020, and (c) 2002–2020.

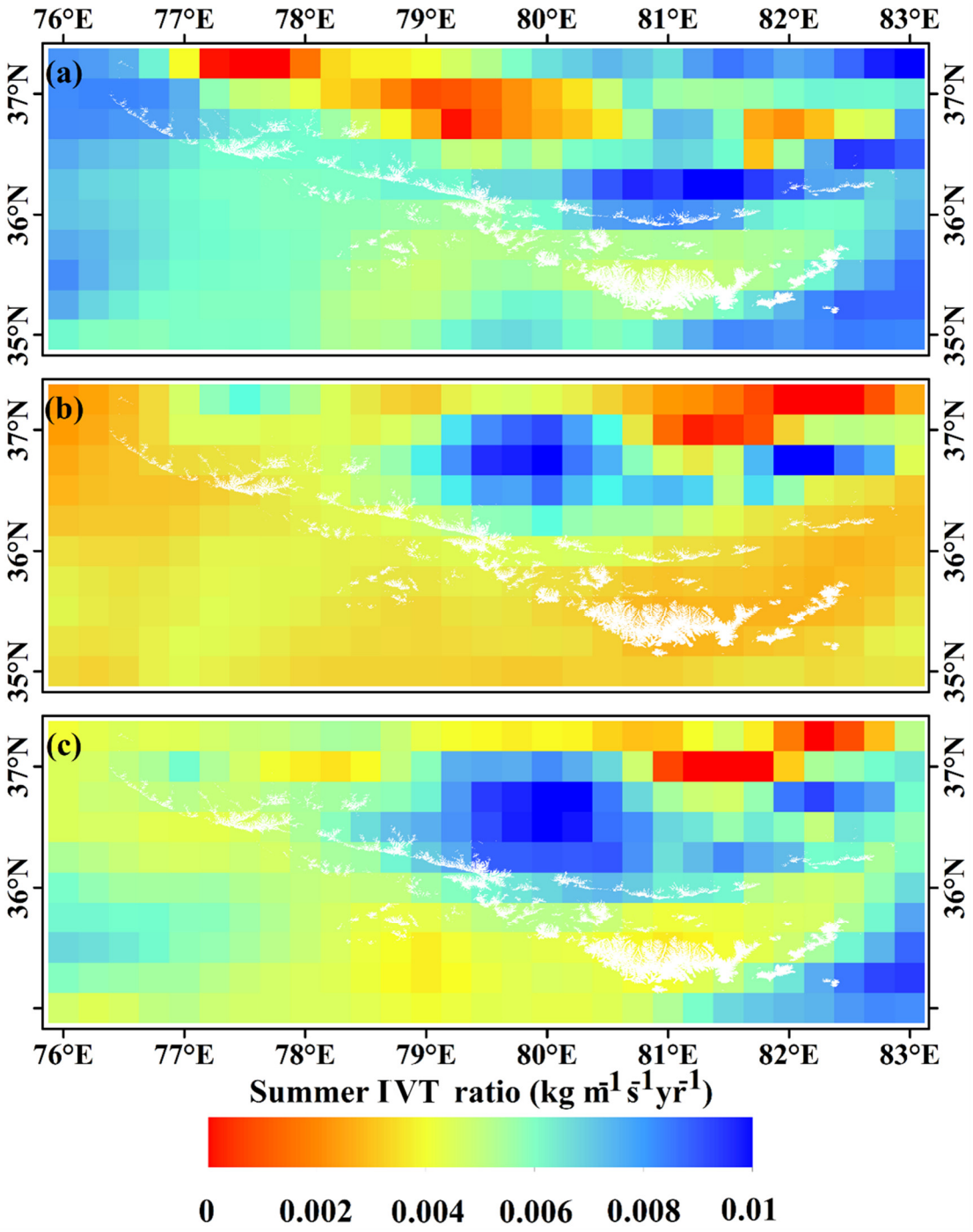

Figure S19. Annual IVT JJA ratio trend per pixel in WK during (a) 2002–2011, (b) 2011–2020, and (c) 2002–2020.

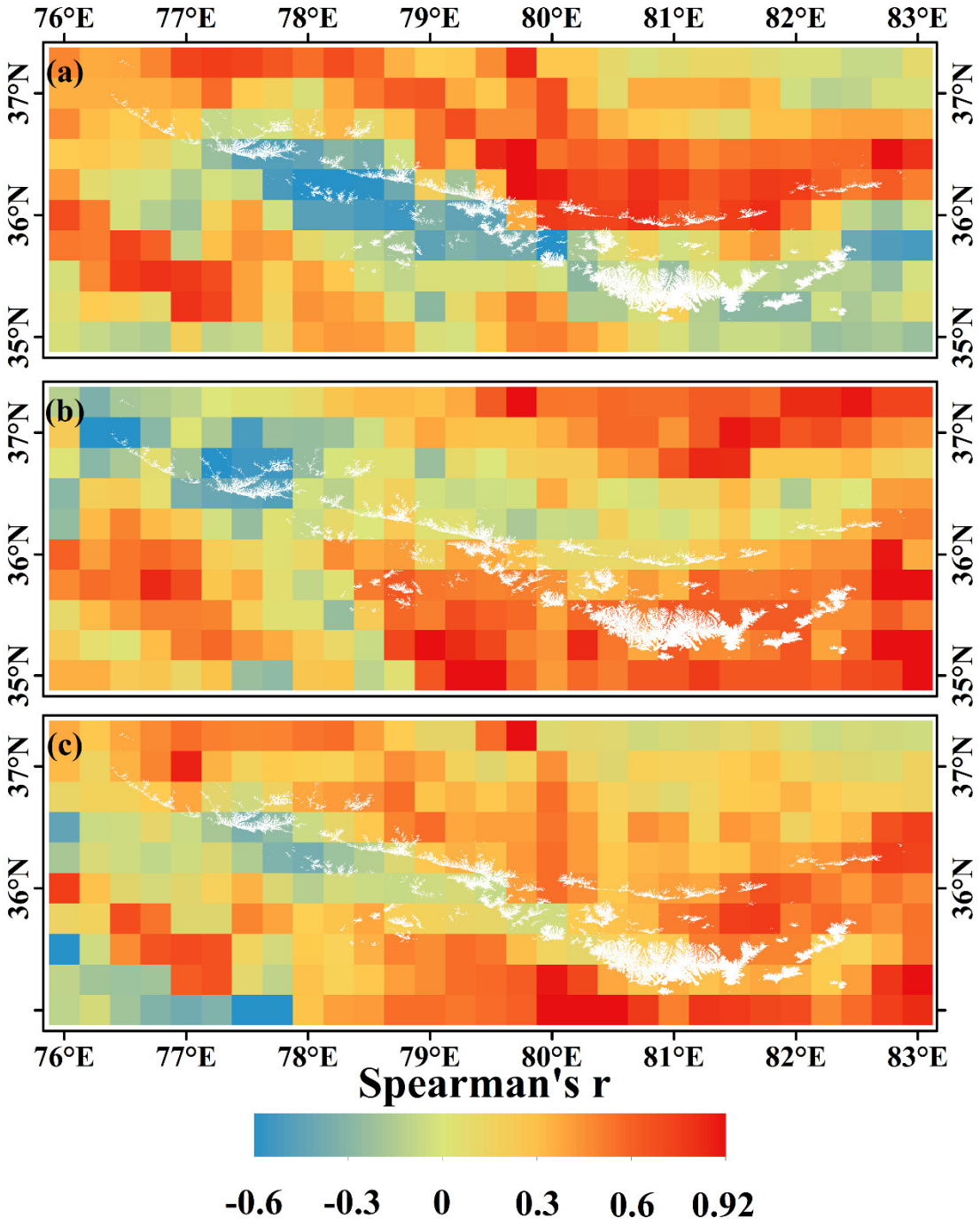

Figure S20. Correlation efficient (Spearman's R) of annual surface temperature per pixel in WK during (a) 2002–2011, (b) 2011–2020, and (c) 2002–2020.

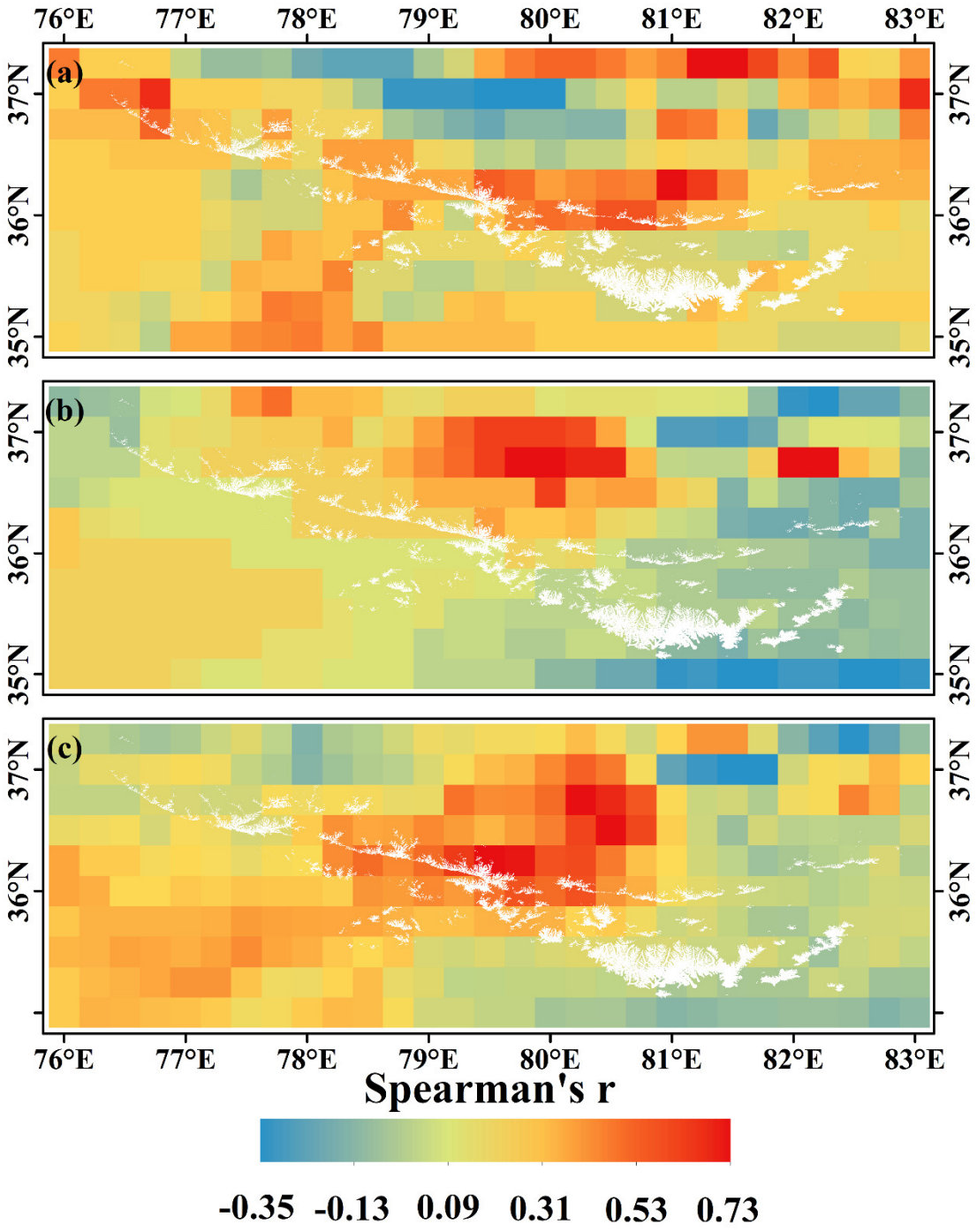

Figure S21. Correlation efficient (Spearman's R) of annual IVT JJA ratio per pixel in WK during (a) 2002–2011, (b) 2011–2020, and (c) 2002–2020.

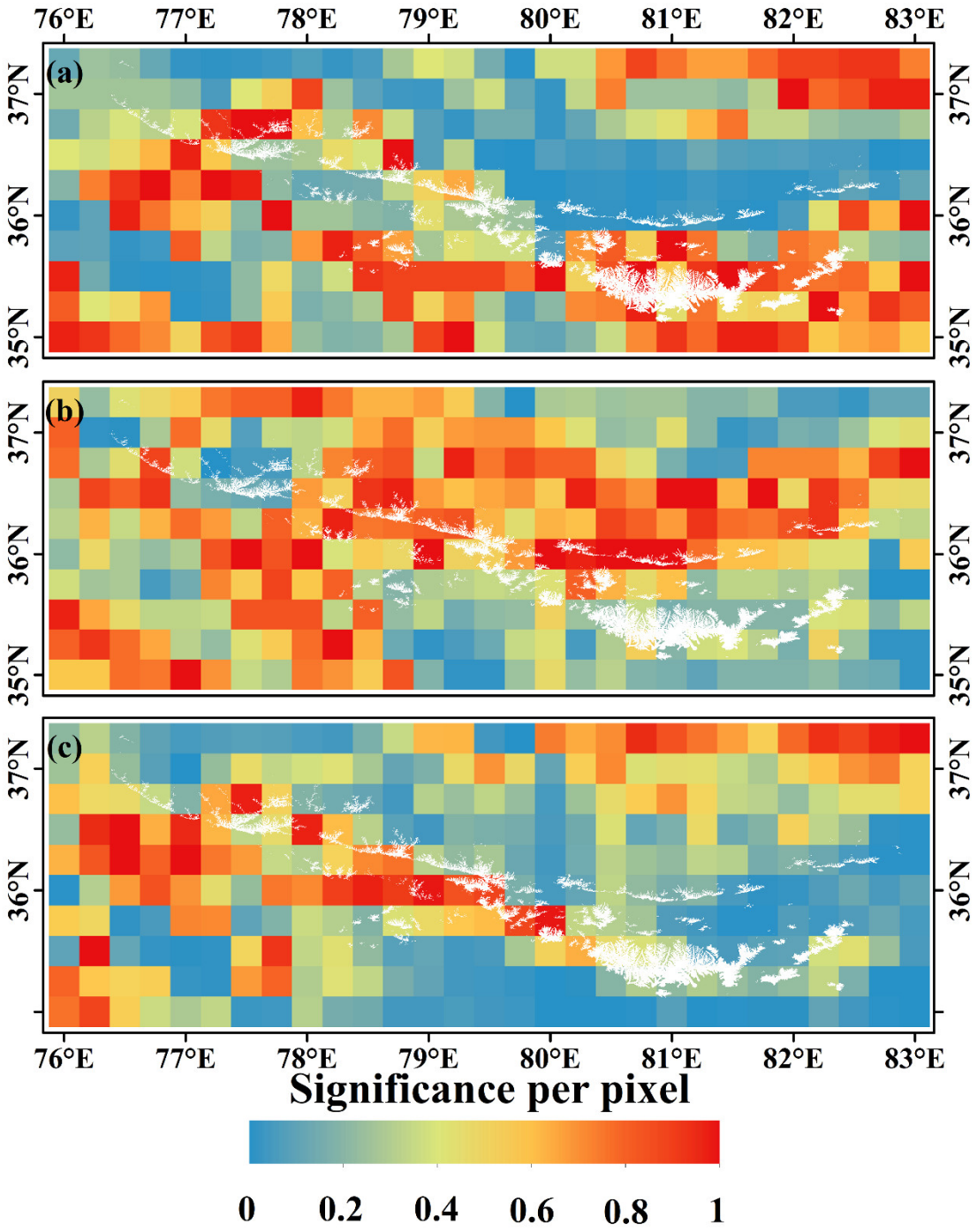

Figure S22. Significance (*p*-value) of annual mean surface temperature per pixel in WK during (a) 2002–2011, (b) 2011–2020, and (c) 2002–2020.

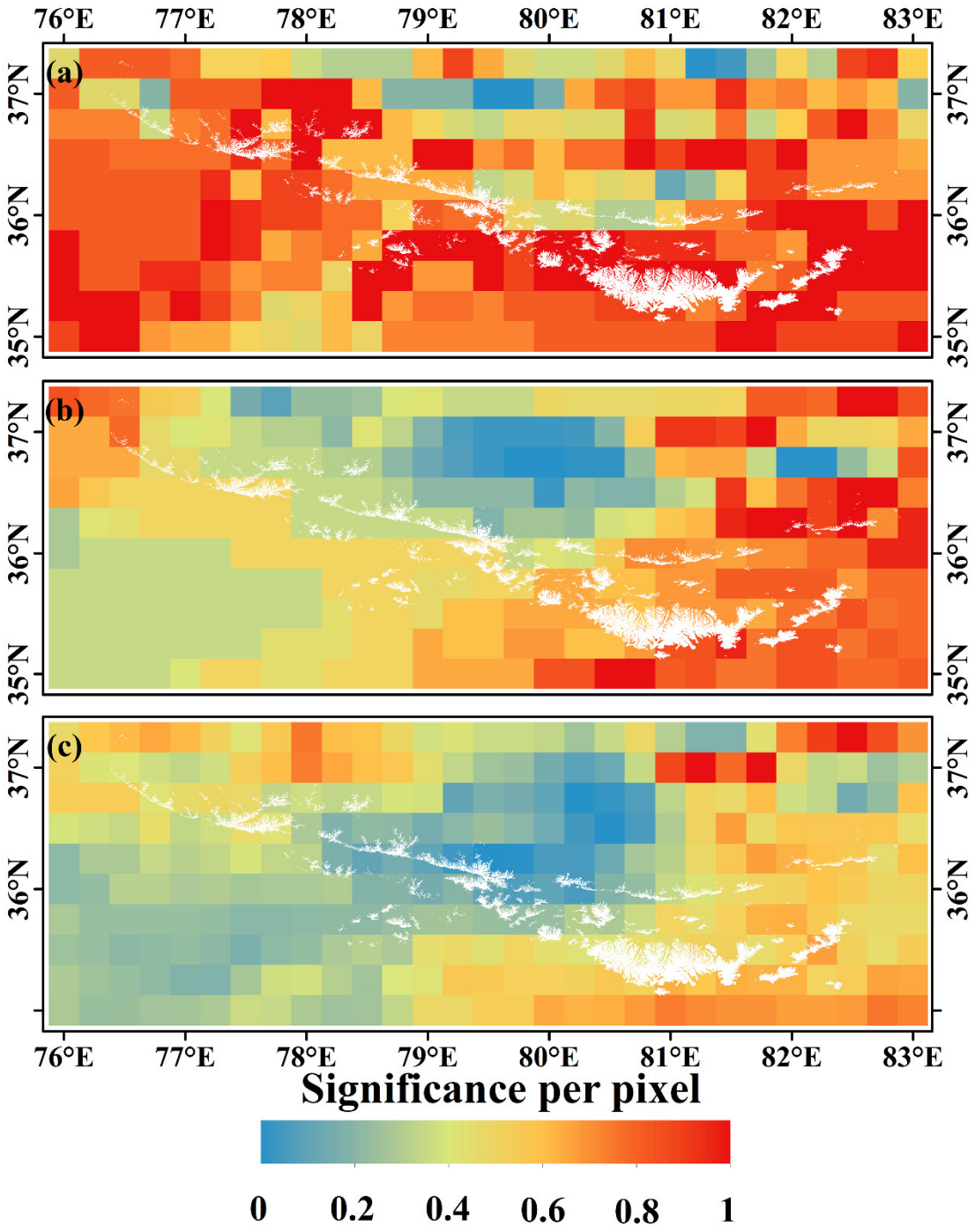

Figure S23. Significance (*p*-value) of annual JJA IVT ratio per pixel in WK during (a) 2002–2011, (b) 2011–2020, and (c) 2002–2020.

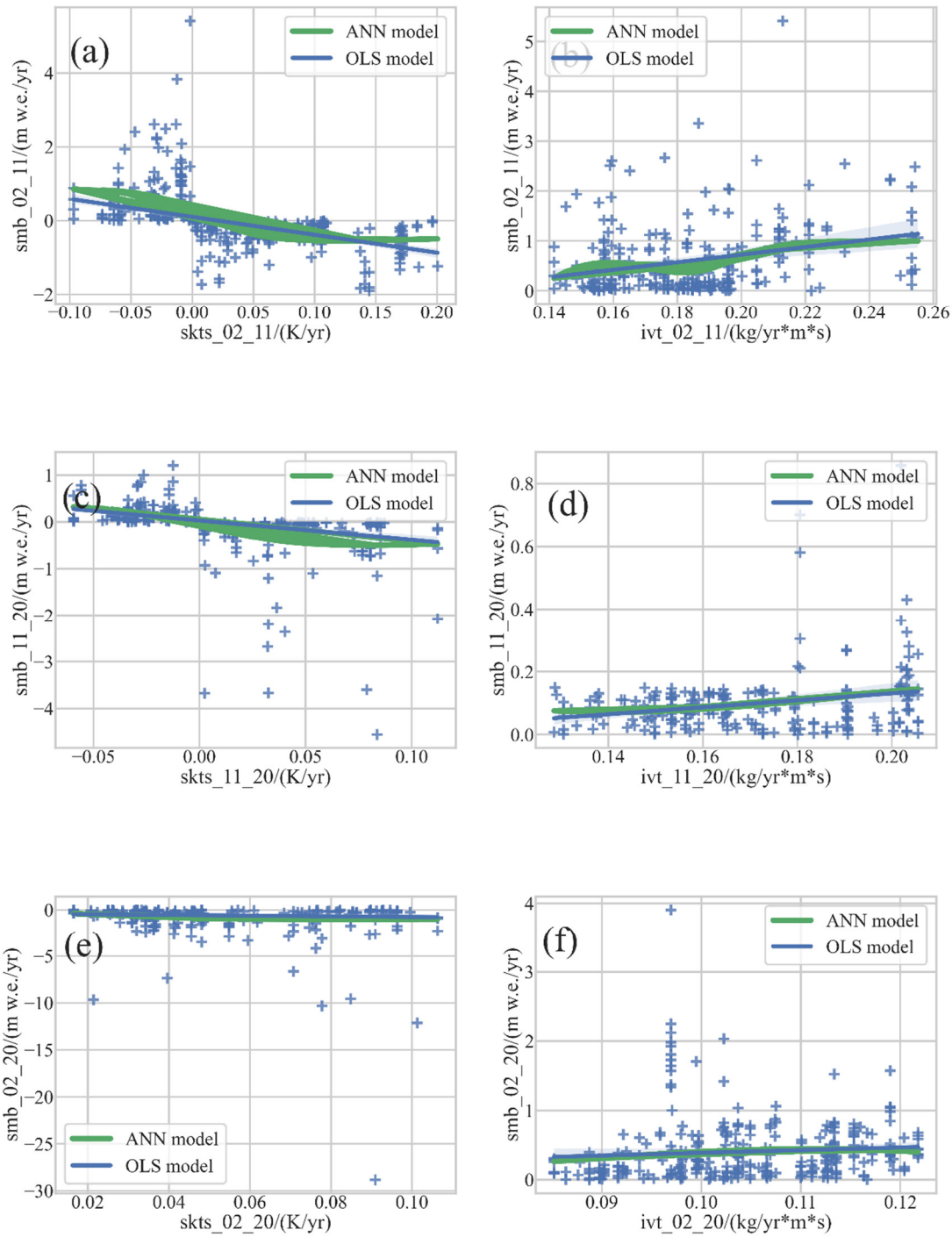

Figure S24. Correlation (Spearman's R) and significance (*p*-value) between glacier SMB and meteorological factors (JJA surface temperature and annual IVT) in WK during (a) and (b) 2002–2011, (c) and (d) 2011–2020, (e) and (f)2002–2020.

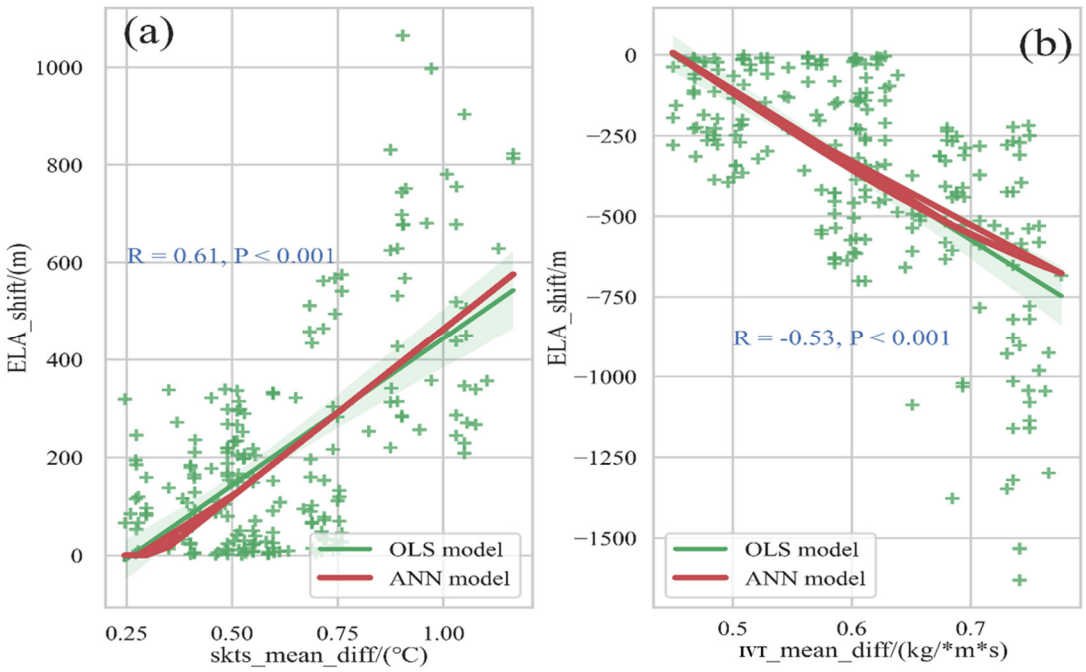

Figure S25. Correlation (Spearman's R) and significance (*p*-value) between glacier ELAs shift and climatic factors: (a) JJA surface temperature, and (b) annual IVT in WK during 2002–2020.

Supplementary Tables

Year	Image number	Glacier area covered (km^2)	Glacier number covered
2001	7	1773.934	199
2002	10	954.858	153
2003	8	2336.375	160
2004	4	737.702	48
2005	3	274.319	55

Table S1. The number of ASTER images for different years from 2001–2005. Glacier counts and area (> 2 km^2) were shielded by ASTER images in each year during this period.

Year	Image number	Glacier area covered (km^2)	Glacier number covered
2009	2	273.343	39
2010	6	1391.085	143
2011	10	1684.679	200
2012	8	2596.211	206
2013	1	131.87	27

Table S2. The number of ASTER imagers for different years from 2009–2013. Glacier counts and area (> 2 km^2) were shielded by ASTER images in each year during this period.

Year	Image number	Glacier area covered (km^2)	Glacier number covered
2018	3	1609.954	62
2019	15	2744.318	331
2020	9	1595.667	193
2021	1	127.249	29

Table S3. The number of ASTER images for different years from 2018–2021. Glacier counts and area (> 2 km^2) were shielded by ASTER images in each year during this period.

Periods	Correlation and significance	Sample number	Glacier SMB-sensitivity model result
2002–2011	JJA skin temperature: R = -0.75, P < 0.001	333	$\frac{\Delta b}{\Delta t} = -0.38\Delta T + 0.22\Delta P$
	IVT: R = 0.28, P < 0.001	252	
2011–2020	JJA skin temperature: R = -0.72, P < 0.001	242	$\frac{\Delta b}{\Delta t} = -0.16\Delta T + 0.07\Delta P$
	IVT: R = 0.24, P < 0.001	210	
2002–2020	JJA skin temperature: R = -0.18, P < 0.01	224	$\frac{\Delta b}{\Delta t} = -0.13\Delta T + 0.45\Delta P$
	IVT: R = 0.25, P < 0.001	302	

Table S4. Correlation coefficients (R) and significances (*p*-value) between glacier mass balance and climatic factors (JJA surface temperature and annual IVT) for three periods (2002–2011, 2011–2020, and 2002–2020).

Periods	Correlation and significance	Sample number	Glacier ELAs-sensitivity model result
2002–2020	JJA skin temperature: R = 0.61, P < 0.001	203	$\Delta\mathrm{ELA} = 154.66\ \Delta\mathrm{T} - 121.57\ \Delta\mathrm{P}$
	IVT:	221	

R = -0.64, P < 0.001

Table S5. Correlation coefficient (R) and significance (*p*-value) between glacier ELAs shifts and climatic factors (JJA surface temperature and annual IVT) during the period 2002–2020.

Supplementary References

1. Dehecq, A.; Gourmelen, N.; Gardner, A.S.; Brun, F.; Goldberg, D.; Nienow, P.W.; Berthier, E.; Vincent, C.; Wagnon, P.; Trouvé, E. Twenty-first century glacier slowdown driven by mass loss in High Mountain Asia. *Nat. Geosci.* **2019**, *12*, 22–27.
2. Herreid, S.; Pellicciotti, F. The state of rock debris covering Earth's glaciers. *Nat. Geosci.* **2020**, *13*, 621–627.
3. Braun, M.H.; Malz, P.; Sommer, C.; Farías-Barahona, D.; Sauter, T.; Casassa, G.; Soruco, A.; Skvarca, P.; Seehaus, T.C. Constraining glacier elevation and mass changes in South America. *Nat. Clim. Change* **2019**, *9*, 130–136.
4. Sakai, A.; Fujita, K. Contrasting glacier responses to recent climate change in high-mountain Asia. *Sci. Rep.* **2017**, *7*, 1–8.
5. Bolibar, J.; Rabatel, A.; Gouttevin, I.; Zekollari, H.; Galiez, C. Nonlinear sensitivity of glacier mass balance to future climate change unveiled by deep learning. *Nat. Commun.* **2022**, *13*, 1–11.
6. Bolibar, J.; Rabatel, A.; Gouttevin, I.; Galiez, C.; Condom, T.; Sauquet, E. Deep learning applied to glacier evolution modelling. *Cryosphere* **2020**, *14*, 565–584.
7. Caidong, C.; Sorteberg, A. Modelled mass balance of Xibu glacier, Tibetan Plateau: Sensitivity to climate change. *J. Glaciol.* **2010**, *56*, 235–248.
8. Sagredo, E.A.; Rupper, S.; Lowell, T.V. Sensitivities of the equilibrium line altitude to temperature and precipitation changes along the Andes. *Quat. Res.* **2014**, *81*, 355–366.
9. McGrath, D.; Sass, L.; O'Neel, S.; Arendt, A.; Kienholz, C. Hypsometric control on glacier mass balance sensitivity in Alaska and northwest Canada. *Earth's Future* **2017**, *5*, 324–336.
10. Dussaillant, I.; Berthier, E.; Brun, F.; Masiokas, M.; Hugonnet, R.; Favier, V.; Rabatel, A.; Pitte, P.; Ruiz, L. Two decades of glacier mass loss along the Andes. *Nat. Geosci.* **2019**, *12*, 802–808.
11. Hugonnet, R.; McNabb, R.; Berthier, E.; Menounos, B.; Nuth, C.; Girod, L.; Farinotti, D.; Huss, M.; Dussaillant, I.; Brun, F.; et al. Accelerated global glacier mass loss in the early twenty-first century. *Nature* **2021**, *592*, 726–731.